Microstructure and nonbasal-plane growth of epitaxial Ti_2AlN thin films

M. Beckers,[a] N. Schell, R. M. S. Martins, A. Mücklich, and W. Möller
Institute of Ion Beam Physics and Materials Research, Forschungszentrum Rossendorf, P.O. Box 510119, 01314 Dresden, Germany

L. Hultman
Thin Film Physics Division, Department of Physics, Chemistry and Biology (IFM), Linköping University, Linköping SE-581 83, Sweden

(Received 8 September 2005; accepted 2 December 2005; published online 1 February 2006)

Thin films of the $M_{n+1}AX_n$ (*MAX*) phase (*M*: early transition metal; *A*: *A*-group element; *X*: C and/or N; $n=1$–3) Ti_2AlN were epitaxially grown onto single-crystal MgO(111) and MgO(100) substrates by dc reactive magnetron cosputtering from Ti and Al targets in an Ar/N_2 gas mixture at a temperature of 690 °C. To promote the nucleation of the *MAX* phase, a fcc $(Ti_{0.63}Al_{0.37})N$ seed layer was deposited before changing to Ti_2AlN growth parameters. The nucleation processes have been studied by real-time *in situ* specular x-ray reflectivity. Independent of substrate orientation, the seed layer shows no roughening until its final thickness of approximately 100 Å, indicating pseudomorphic layer-by-layer growth. The *MAX* phase shows heteroepitaxial layer-by-layer growth on MgO(111), with increased surface roughening up to approximately 200 Å, whereas on MgO(100) the growth mode changes to Volmer-Weber-type already after three monolayers. X-ray scattering in Bragg-Brentano geometry of the final, approximately 1000 Å thick, Ti_2AlN film reveals lattice parameters of $c=13.463$ Å and $a=2.976$ Å on the MgO(111) substrate and $c=13.740$ Å and $a=2.224$ Å on the MgO(100) substrate. From pole figure measurements the orientational relationship between film and substrate lattice was determined to be $MgO\{111\}\langle 110\rangle // Ti_2AlN\{10\bar{1}2\}\langle \bar{1}2\bar{1}0\rangle$, regardless of the substrate orientation. This tilted, nonbasal-plane growth leads to a threefold grain orientation of Ti_2AlN along the $MgO\langle 110\rangle$ directions and a polycrystalline morphology confirmed by cross-sectional transmission electron microscopy. The growth can be assumed to take place in a lateral step-flow mode, i.e., emerging low surface free-energy (0001) planes, on which arriving atoms can diffuse until finding a step where they are bound to *A* facets. This growth process is irrespective of orientational relationship between substrate and film. However, in the present low-temperature case the partitioning of arriving Al and Ti atoms during nucleation is suppressed, which as a result of interfacial adaptation between substrate and film induces standing *a*-type planes during growth. © *2006 American Institute of Physics*. [DOI: 10.1063/1.2161943]

I. INTRODUCTION

The $M_{n+1}AX_n$ (*MAX*) phases[1] are a family of layered, hexagonal carbides and nitrides, where *M* is an early transition metal, *A* is an *A*-group element (mostly IIIA and IVA), and *X* is either C or N. In principle the $P63/mmc$ space-grouped $M_{n+1}AX_n$ phases are built by slabs of edge sharing $[MX_6]$ octahedrons, identical to those found in the rock salt structure of the corresponding carbides/nitrides. The C or N atoms occupy the octahedral interstitial sites between the closed packed layers of the transition-metal atoms, separated from each other by layers of the *A*-group element. In the 211 configuration reported here, every third layer is constituted by *A*-group atoms, every fourth in the 312 configuration, etc.

Due to their close structural relationship to the corresponding *MX* binary compounds the $M_{n+1}AX_n$ phases show comparable behavior. This includes high stiffness, thermodynamic stability at high temperatures, and good electrical as well as thermal conductivity. However, since the *M*–*A* bond is relatively weak, the mechanical properties are extremely anisotropic and variable. $M_{n+1}AX_n$ phases deform by the formation of kink and shear bands so that dislocations glide exclusively on the basal planes and are arranged in kink boundaries. As a consequence, $M_{n+1}AX_n$ phases are readily machinable, relatively soft along the *a* axis, and unusually damage tolerant. Furthermore, on the microscopic scale ultralow friction coefficients of 0.005 along the basal planes have been reported.

The nucleation of a bulk $M_{n+1}AX_n$ phase—Ti_2AlN—has been reported in 1963 by Jeitschko *et al.*,[2] and already in 1972 chemical vapor deposited Ti_3SiC_2 had been reported to show anomalous behavior for a carbide.[3] However, the production of pure single-phase bulk material was not observed until the work of Barsoum and El-Raghy, who reported the results on the compound Ti_3SiC_2.[1] Up to this day some 50 *bulk* $M_{n+1}AX_n$ phase compounds[4] have been produced, which partly have already found their way into commercialization.[5] For the Ti–Al–N system, $M_{n+1}AX_n$ structured compounds of the composition Ti_2AlN (Ref. 2) and Ti_4AlN_3 (Ref. 6) have been reported. Ti_4AlN_3 was assumed to be $Ti_3Al_2N_2$, but cross-sectional transmission electron microscopy (TEM) characterization by Barsoum *et al.*[7] proved the right stoichiometry to be Ti_4AlN_3 including a $M_{n+1}AX_n$ phase atomic configuration. Recent theoretical calculations published by Holm *et al.*[8] predict another, metastable Ti_3AlN_2 phase. Us-

[a]Electronic mail: m.beckers@fz-rossendorf.de

ing *ab initio* calculations, Music *et al.*[9] showed that for boron-based perovskites RM_3B, where R and M are rare earth and 4*d* metals, respectively) the coupling between M–R and M–B layers in RM_3B can be switched from predominantly covalent ionic to metallic in character by varying the population of the M *d* shells. Based on the electron density distribution resemblance to the *MAX* phases,[10] it is reasonable to assume that alternating covalent-ionic and metallic bondings in these compounds may give rise to similar properties as observed for *MAX* phases. Hence, though the original definition of the $M_{n+1}AX_n$ phase took only carbon and nitrogen into account as covalent bonding partners, this definition appears to require extension for further research.

However, all these publications are related to either theoretical calculation or synthesis of bulk material, whereas the $M_{n+1}AX_n$ phase's unique mechanical properties could also be profitable for thin-film applications, such as high-temperature wear protection. Therefore, it has been a challenge to produce them by thin-film deposition techniques. Seppänen *et al.*,[11] as well as Palmquist *et al.*,[12] demonstrated the general feasibility of carbidic $M_{n+1}AC_n$ phase deposition, followed by articles on Ti_2AlC and Ti_3AlC_2.[13] A more detailed report on Ti_3SiC_2 grown by sputter deposition from elemental targets has lately been published by Emmerlich *et al.*[14] Finally, also the nucleation of $Ti_{n+1}GeC_n$ thin films has been reported.[15] For the sputter deposition of nitride $M_{n+1}AN_n$ thin films, nitrogen in comparison with carbon cannot be provided by sputtering from an elemental target, but has to be introduced by reactive sputtering in a very narrow process window. Consequently, only very recently Joelsson *et al.* reported on the deposition of single-crystal Ti_2AlN.[16] They used a reactive sputtering process from a compound 2Ti:Al target, and deposited directly onto a MgO(111) wafer at a deposition temperature of 830 °C. In the present work reactive cosputtering from metallic Ti and Al targets is employed at a significantly lower substrate temperature of 690 °C. *In situ* x-ray characterization was carried out in order to understand the nucleation and growth process for both a $Ti_{1-x}Al_xN$ seed layer and the Ti_2AlN *MAX* phase film, accompanied by postdeposition x-ray diffraction and cross-sectional transmission electron microscopy (XTEM).

II. EXPERIMENTAL DETAILS

The Ti_2AlN films were deposited in a deposition chamber mounted into the six-circle goniometer of the synchrotron radiation beamline ROBL (BM20) at European Synchrotron Radiation Facility (ESRF), Grenoble. A detailed description of this chamber is given in Ref. 17. It is equipped with Kapton windows for x-ray penetration and two commercially available balanced magnetrons with 1 in. diameter targets. The magnetrons are tilted 30° away from the substrate surface normal at a target-substrate distance of 100 mm. Chimneys in front of each magnetron and pneumatically driven blade shutters avoid cross contamination and ensure accurate determination of deposition times. Ti and Al disks with a 99.999% purity were used as targets. The substrates were polished $10\times10\times0.5$ mm^3 MgO(100) and MgO(111) wafers which were reconstructed, cleaned, and thermally degassed by heating to 690 °C for 1 h. The temperature was recorded by a chromel-alumel thermocouple clamped aside the substrate holder. A substrate bias U_B of −30 V was applied during all depositions. The base pressure at the deposition temperature of 690 °C was $\sim8\times10^{-5}$ Pa. For the fcc $Ti_{1-x}Al_xN$ seed layer, Ar and N_2 fluxes of 2.76 and 1.38 sccm (standard cubic centimeter per minute) were chosen, respectively, leading to a working pressure of 0.35 Pa. The Ti and Al magnetrons were driven at 60 and 20 W, respectively, leading to a composition of $(Ti_{0.63}Al_{0.37})N$, which is close to the nominal corresponding M/A ratio of Ti_2AlN. In order to achieve stable growth conditions for the Ti_2AlN *MAX* phase film, the deposition pressure was increased to 0.8 Pa at Ar and N_2 fluxes of 7.94 and 0.48 SCCM, respectively. The Ti and Al magnetrons were then driven at 80 and 26 W, respectively, leading to a Ti/Al ratio of 2/1 as required for the Ti_2AlN *MAX* phase and as established in preceding work.[18]

Monochromatized x rays of 12.915 keV ($\lambda=0.961$ Å) were employed to study the film growth *in situ* in two different scattering geometries: (1) low angle specular reflectivity either time resolved at a fixed incidence angle to determine the growth mode, or scanned in coplanar scattering geometry for the determination of the film thickness and (2) large angle x-ray diffraction (XRD) in Bragg-Brentano geometry in order to determine the off-plane lattice parameter. The time-resolved specular reflectivity signal resembles the technique of reflective high-energy electron diffraction (RHEED) and thus can be used to observe changes in the surface morphology during growth on an atomic scale,[19–21] from which the growth mode of the developing film can be derived.

The microstructure and texture of the final film were investigated using a combination of pole figure measurements and XTEM. The pole figures were recorded at a laboratory source with Cu $K\alpha$ radiation. The XTEM analyses were performed in a Philips CM300 microscope with a LaB_6 filament at 300 keV. Cross-sectional specimens were prepared by gluing two samples film to film and cutting vertical sections which were mechanically ground and subsequently thinned down by ion milling using a 5 keV Ar^+-ion beam. The final film composition was examined by Rutherford backscattering spectroscopy (RBS), using a 1.7 MeV He^+ beam at normal incidence and a surface barrier detector set at 170° scattering angle. The backscattered spectra were analyzed by spectrum fitting using the SIMNRA 5.0 code.[22]

III. RESULTS

On the two different substrate orientations, MgO(111) and MgO(001), an approximately 1000-Å-thick Ti_2AlN film was deposited on top of an ~100-Å- thick $(Ti_{0.63}Al_{0.37})N$ seed layer, keeping all other deposition parameters constant. For a precise elemental analysis by RBS without overlapping of nitrogen and oxygen signals, layers with identical deposition parameters were deposited onto pyrolytic graphite. The fitted compositions were $Ti_{0.49\pm0.02}Al_{0.25\pm0.02}N_{0.26\pm0.04}$ and thereby equal to the desired composition of $Ti_{0.50}Al_{0.25}N_{0.25}$ within the experimental errors. The maximum oxygen con-

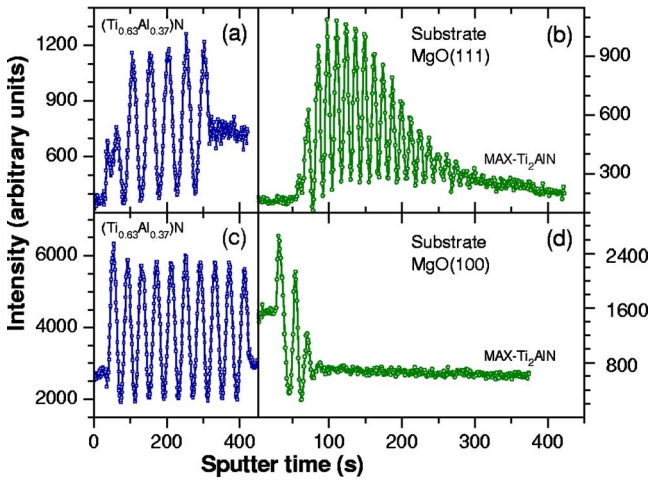

FIG. 1. (Color online) Time-dependent *in situ* specular x-ray reflectivity of the fcc $(Ti_{0.63}Al_{0.37})N$ seed layers [(a) and (c)] and *MAX* phase Ti_2AlN [(b) and (d)] on the substrates MgO(111) [(a) and (b)] and MgO(100) [(c) and (d)]. The incidence and scattering angles were fixed at $\Theta/2\Theta=1.8°/3.6°$ [(a) and (b)] and $\Theta/2\Theta=2.1°/4.2°$ [(c) and (d)]. The oscillatory behavior for the deposited seed layers as well as the Ti_2AlN films on top are a fingerprint of *layer-by-layer* growth. The decreasing amplitudes of those oscillations reveal increasing roughness or island growth, which is more pronounced for the Ti_2AlN film on MgO(100) (d).

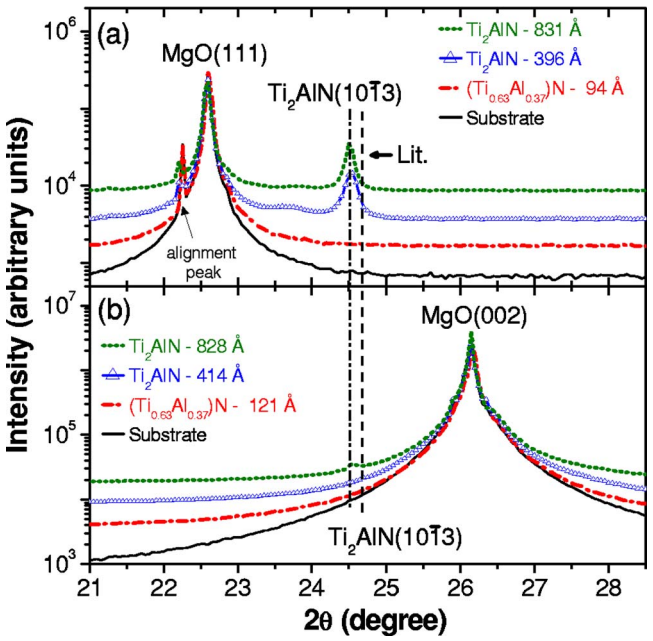

FIG. 2. (Color online) *In situ* x-ray diffractograms recorded in vertical Bragg-Brentano geometry on the substrates MgO(111) (a) and MgO(100) (b) after deposition of the seed layer and two Ti_2AlN film deposition steps of approximately 400 Å each. (The experimental curves follow the legend's order. The vertical dashed-dotted line in the graph is only a guide to the eye. The additional peak seen in the spectra is a measuring artifact. For the time-resolved XRR the samples have been aligned to the sample surface and *not* to the MgO crystal planes. A slight miscut of the crystal lattice planes then leads to the observed shoulder in XRD.)

centration was 3 at. %, with a steep decrease from the surface into the film, indicating postdeposition surface oxidation, rather than oxygen contamination *during* the growth process.

A. *In situ* characterization of the nucleation

Figure 1 shows the time-dependent x-ray specular reflectivity for both the seed layer [(a) and (c)] and the actual Ti_2AlN *MAX* phase layer [(b) and (d)] on MgO(111) [(a) and (b)] and MgO(100) [(c) and (d)]. The intensity was recorded at intervals of 1 s, starting 30–50 s before the shutter was opened and the deposition began. Clear intensity oscillations are depicted for the seed layers. The oscillation amplitude does not diminish during deposition; hence for both crystallographic substrate orientations a smooth layer-by-layer (step flow) growth onto the MgO can be deduced, as expected from epitaxial growth of pure TiN onto MgO(111) single-crystal substrates, reported in 1985 by Johannson *et al.*[23] and extended by *in situ* Auger electron spectroscopy by Mirkarimi *et al.*, who studied layer-by-layer growth of TiN/VN superlattices deposited onto MgO(100).[24] Recent publications used *in situ* scanning tunneling microscopy to analyze the growth of TiN onto atomically flat TiN(111) and TiN(100),[25] which allows calculating activation energies for adatom formation and surface diffusion on both surfaces. This led to an adapted step-flow model for the homoepitaxial growth of TiN(111).[26]

After nucleation of the cubic seed layer, the deposition was interrupted and the deposited film was characterized by x-ray reflectometry (XRR). Fitting the data with the Bede REFS computer code[27] yields layer thicknesses of 94 Å and—due to longer deposition time—121 Å on MgO(111) and MgO(100), respectively. This corresponds to a quite low growth rate of 0.3 Å/s, which specially enhances the layer-by-layer growth as will be shown elsewhere. Combining the growth rate and the deposition time, each oscillation in the specular reflectivity can be attributed to one lattice constant of the $(Ti_{0.63}Al_{0.37})N$. Hence, regardless of substrate orientation a perfect cube-on-cube heteroepitaxial relation $(Ti_{0.63}Al_{0.37})N\{100\}\langle 100\rangle//MgO\{100\}\langle 100\rangle$ for the seed layer can be assumed (taking into account the orientation results as represented in Fig. 2). This is due to the low lattice mismatch of only 0.74% between $(Ti_{0.63}Al_{0.37})N$ [4.18 Å—extrapolated according to Vegard's law—which is valid for this system[28]—between TiN and cubic AlN (Ref. 29) and MgO [4.211 Å (Ref. 30)].

Figures 1(b) and 1(d) show that the growth mode of the Ti_2AlN *MAX* phase depends on the substrate and thereby seed layer orientation. Even after interrupting the deposition process for characterization for about 1 h, the $M_{n+1}AX_n$ phase nucleation onto the seed layer proceeds again in a layer-by-layer mode. In the case of a MgO(111) substrate, the oscillations are clearly visible for more than 15 monolayers [Fig. 1(b)], while for MgO(100) [Fig. 1(d)] the oscillations die out already after 3 monolayers. This signifies a pronounced kinetic roughening, in particular, for the latter case, i.e., a Stranski-Krastanov-like growth mode. The deposition rate of the Ti_2AlN *MAX* phase for both substrate orientations was determined by XRR to be 1.3 Å/s, explaining the smaller oscillation period compared to the $(Ti_{0.63}Al_{0.37})N$ seed layer.

B. *In situ* characterization of the crystallization

Besides XRR, after each deposition step XRD was also carried out. The θ-2θ scans, offset for clarity of presentation,

are shown in Fig. 2. For both substrate orientations, after deposition of the seed layer the scattered intensity distribution remains undistinguishable due to the perfect epitaxial nature of the seed layer growth. In contrast, already after the first deposition of ~400 Å *MAX* phase, the $Ti_2AlN(10\bar{1}3)$ peak can clearly be identified on the MgO(111) substrate [Fig. 2(a)] as the only peak resulting from the *MAX* phase. This peak is so close in angle to the Ti_2AlN (0006) peak that in early diffraction data they have not been separated[31] but due to the lack of multiplicity peaks Ti_2AlN (0008), Ti_2AlN (00010), etc., a mixup can be excluded. The same $Ti_2AlN(10\bar{1}3)$ peak is also observed on the MgO(100) substrate [Fig. 2(b)], but only after a second deposition step of another ~400 Å. For later discussions, it should be noted that the lattice spacing of the $Ti_2AlN(10\bar{1}3)$ peak is somewhat increased compared to the literature values as is indicated by the dashed line in Fig. 2. Besides, also the $Ti_2AlN(10\bar{1}2)$ peak would be close to $Ti_2AlN(10\bar{1}3)$; however, it is a highly suppressed reflex due to x-ray selection rules.

C. Pole figures and orientational relationship between MgO and Ti_2AlN

Due to the window limitations of the *in situ* sputter chamber, θ-2θ scans over an angle range of 10°–90° have been performed *ex situ* using a laboratory source. However, no other possible Ti_2AlN peaks in addition to $Ti_2AlN(10\bar{1}3)$ were found, indicating a film with pronounced preferred orientation. In order to clarify the nature of the orientational relationship between the MgO substrate and the Ti_2AlN *MAX* phase, also *ex situ* pole figures were recorded for both substrate orientations (Figs. 3 and 4). Figure 3(a) shows the experimental pole figure for a film deposited onto MgO(111) substrate, recorded in the $Ti_2AlN(10\bar{1}3)$ Bragg peak. Due to the immediate vicinity of the Ti_2AlN (0006) and MgO(111) as well as MgO(100) reflexes, the pole figure comprises orientation distributions of all these four lattice planes. For all cluster points within the experimental pole figure (Fig. 3(a)], θ-2θ scans were executed, which showed only the MgO substrate and $Ti_2AlN(10\bar{1}3)$ Bragg peaks, except from the cluster points at $\chi \sim 60°$, and $\phi=0°$, 120°, and 240°. Here, a peak at $2\theta=13°$ was observed, which is close to the Ti_2AlN (0002) Bragg reflex. Hence, a pole figure on that peak was recorded, which is shown in Fig. 3(b). It clearly shows three distinct cluster points at $\chi \sim 60°$, and $\phi=0°$, 120°, and 240°. Thus, the (0001) basal planes of the Ti_2AlN are tilted away from the surface normal by ~60° with threefold symmetry around the substrate normal axis.

Figure 3(c) shows a schematic theoretical pole figure derived from the stereographic projection of the Ti_2AlN (Ref. 31) and MgO (Ref. 30) crystallographic patterns using the CARINE 3.1 software.[32] If we assume a single-crystal Ti_2AlN and MgO, the (111) substrate orientation leads to the central MgO(111) pole and three MgO{100} poles at a tilting angle $\chi=54.7°$ and azimuth angles $\phi=0°$, 120°, and 240°. Three other MgO{111} poles lie at $\chi=70.53°$, each of them opposite of the corresponding MgO{100} pole [for clarity

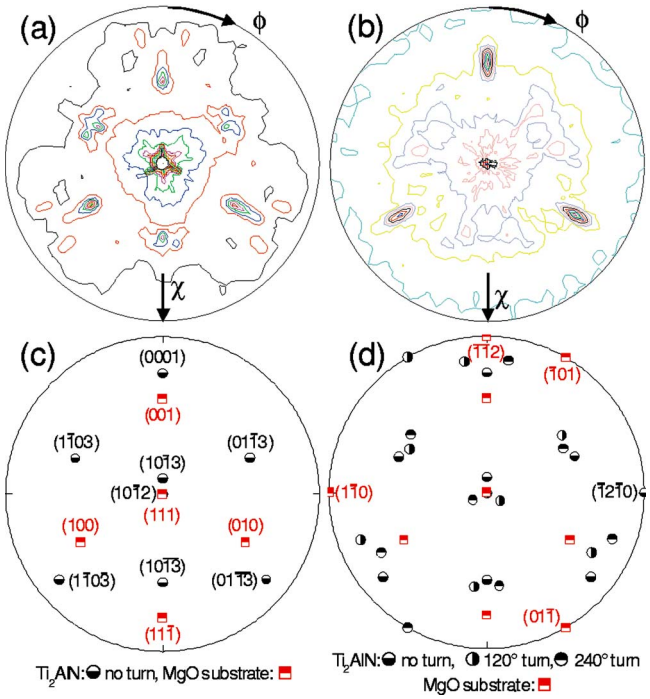

FIG. 3. (Color online) Pole figures of *MAX* phase Ti_2AlN grown on MgO(111) substrate, nominally measured on the Bragg peaks $Ti_2AlN(10\bar{1}3)$ (a) and Ti_2AlN (0002) (b). The stereographic projection (c) shows the theoretical poles of $Ti_2AlN\{10\bar{1}3\}$,$\{10\bar{1}2\}$, {0001}, and $\{\bar{2}1\bar{1}0\}$ as well as MgO{111}, $\{1\bar{1}0\}$, and $\{\bar{1}\bar{1}2\}$. The experimental pole figure can be obtained by turning the poles for 120° around the MgO[111] direction, as indicated by the symbols (d).

only the MgO(11$\bar{1}$) opposite to the MgO(001) is shown in Fig. 3(c). As seen in Fig. 3(b), close to the MgO(001) pole lies the Ti_2AlN (0001) pole. As a consequence, the $Ti_2AlN(10\bar{1}3)$ pole lies not in the center of the pole figure, but at $\chi=9°$ and $\phi=0°$. Accordingly, within the central position lies the $Ti_2AlN(10\bar{1}2)$ pole. Thus, one can already denote MgO(111)//$Ti_2AlN(10\bar{1}2)$. It should again be noted that the $Ti_2AlN(10\bar{1}3)$ planes are *not* parallel to the substrate

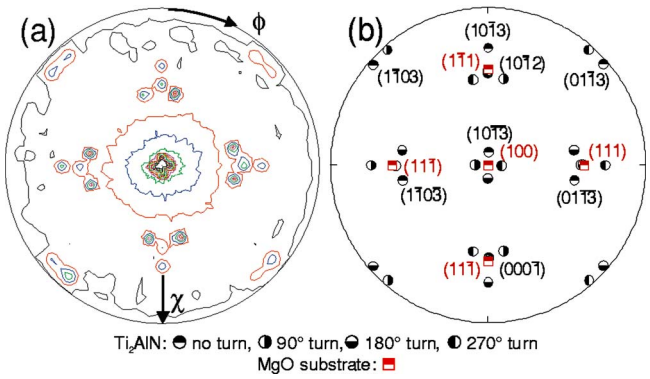

FIG. 4. (Color online) Experimental pole figure of *MAX* phase Ti_2AlN grown on MgO(100) substrate, nominally measured on the Bragg peak $Ti_2AlN(10\bar{1}3)$ (a). The stereographic projection (b) shows the theoretical poles of $Ti_2AlN\{10\bar{1}3\}$,$\{10\bar{1}2\}$, {0001}, and $\{\bar{2}1\bar{1}0\}$ as well as MgO{111}, $\{1\bar{1}0\}$, and $\{\bar{1}\bar{1}2\}$. The experimental pole figure can be obtained by turning the poles for 90° around the four possible MgO⟨100⟩ directions, as indicated by the symbols.

surface, but tilted by ~9°. Thus, the $Ti_2AlN(10\bar{1}3)$ peaks recorded in the *in situ* coplanar scattering geometry are just the projection along the surface normal, being detected within the angular divergence of the x-ray geometry, and do not represent the real thin-film orientation. That real off-plane orientation is $\{10\bar{1}2\}$, but hardly observable in XRD due to the x-ray selection rules. Within Fig. 3(a), permutation of the first three Miller indices yields five additional $Ti_2AlN\{10\bar{1}3\}$ poles, positioned as indicated by the indices and the symbol (◒). Additionally, this figure must also be turned around by 120° and 240° due to the threefold symmetry of the Ti_2AlN (0002) peak. This makes up for another 14 [two times (6+1)] cluster points. For clarity, the indexing of these collective points that are shown in Fig. 3(d) has been omitted. Each in-plane turn of 120° is indicated by the symbols (◑) and (◓). The picture obtained describes all the features of the experimental pole figures, and also displays the orientational relationship between the MgO substrate, the $(Ti_{0.63}Al_{0.37})N$ seed layer, and the Ti_2AlN *MAX* phase.

The question about the azimuthal orientational relationship can be answered by looking at the poles for $\chi=90°$, where obviously the $MgO(1\bar{1}0)$ and $Ti_2AlN(\bar{1}2\bar{1}0)$ poles overlap. For the cubic MgO the corresponding direction is $[1\bar{1}0]$ and for the Ti_2AlN it is $[\bar{1}2\bar{1}0]$. Since there are three possible MgO⟨110⟩ directions on the MgO(111) surface, the threefold in-plane symmetry of the Ti_2AlN can thus be described by the orientational relation $MgO\{111\}\times\langle 110\rangle//Ti_2AlN\{10\bar{1}2\}\langle\bar{1}2\bar{1}0\rangle$.

Pole figures of the same Bragg peaks have also been recorded for Ti_2AlN *MAX* phase deposited onto MgO(100). The experimental pole figure is shown in Fig. 4(a), and again is comprised of the four different Bragg peaks in close vicinity as mentioned above. Now in the theoretical single-crystal pole figure [Fig. 4(b)], the substrate [100] orientation leads to a central MgO(100) pole and four MgO{111} poles at a tilting angle $\chi=54.7°$ and azimuth angles $\phi=0°$, 90°, 180°, and 270°. The θ-2θ scans showed that all additional cluster points in the experimental pole figure can be reduced to exclusively $Ti_2AlN\{10\bar{1}3\}$ peaks. The central $Ti_2AlN(10\bar{1}3)$ peak is now tilted ~7° away from the substrate normal and by permutation leads to six poles as indexed and marked by the symbol (◓). Additionally, the central peak shows fourfold symmetry around the central MgO(100) pole, so the figure described above has to be turned by 90°, 180°, and 270° as marked by the symbols (◑), (◒), and (◐). Again for clarity reasons the indexing has been omitted in the figure. The obtained picture describes the experimental pole figure and clarifies the orientational relationship. Taking a closer look into the stereographic projection reveals again $Ti_2AlN(10\bar{1}2)$ parallel to the four possible MgO{111} poles, with a threefold orientation of the $Ti_2AlN\{10\bar{1}3\}$ poles around each of them. In conclusion the orientational relationship can again be denoted as $MgO\{111\}\times\langle 110\rangle//Ti_2AlN\{10\bar{1}2\}\langle\bar{1}2\bar{1}0\rangle$, or taking the actual substrate orientation into account $MgO\{100\}\langle 110\rangle//Ti_2AlN\{10\bar{1}4\}\times\langle\bar{1}2\bar{1}0\rangle$, and is thus persistent regardless of choice of substrate orientation.

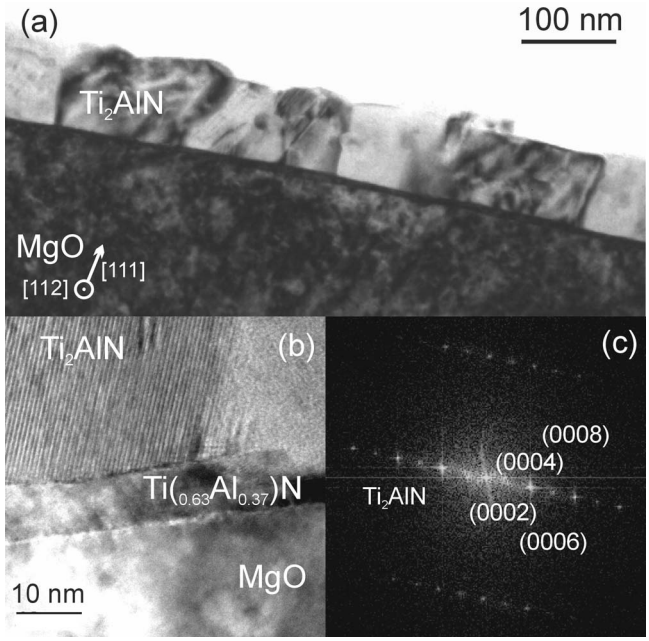

FIG. 5. XTEM micrograph of Ti_2AlN grown on MgO(111) along the MgO[112] zone axis. (a) shows an overview over the film morphology consisting of large crystal regions. (b) shows a TEM micrograph at the interface with the typical *MAX* phase 2-1-1 layered structure. It is made up by the (000ℓ) planes as confirmed from *d*-spacing calculation by FFT (c).

Besides examining the orientational relationship between substrate and film, also the Ti_2AlN lattice constants were calculated from the coupled θ-2θ scans of each cluster point. The *c*-axis values were calculated from the (0002) and (0006) reflexes, acting as input factor for the *a*-axis calculation from the mixed $(10\bar{1}3)$ peak. The calculations resulted in Ti_2AlN film lattice parameters of $c=13.463$ Å and $a=2.976$ Å on the MgO(111) and $c=13.740$ Å and $a=2.224$ Å on the MgO(100) substrate. The literature values are $c=13.614$ Å and $a=2.989$ Å; hence our *c*-axis values are within approximately 1% deviation from literature. The larger deviation from *a*-axis literature values for the MgO(100) substrate can be understood from the rather unusual in-plane growth of Ti_2AlN on MgO(100) as will be discussed in the subsequent section.

D. XTEM characterization

Figure 5(a) shows a XTEM micrograph from Ti_2AlN deposited on MgO(111) recorded along the MgO[112] zone axis, i.e., along the Ti_2AlN [1210] zone axis. The layer is not single crystalline, but exhibits an equiaxed morphology, with individual epitaxial grains corresponding to Fig. 3, whose sizes are in the dimension of the film thickness, i.e., around 1000 Å. There is a strong diffraction contrast between the individual grains which is due to the threefold in-plane symmetry described above. Additionally, in accordance with the time-resolved specular reflectivity the layer displays high surface roughness, caused by the tilted nonbasal-plane growth. Figure 5(b) shows the interface between one of these grains, the $(Ti_{0.63}Al_{0.37})N$ seed layer and the MgO substrate.

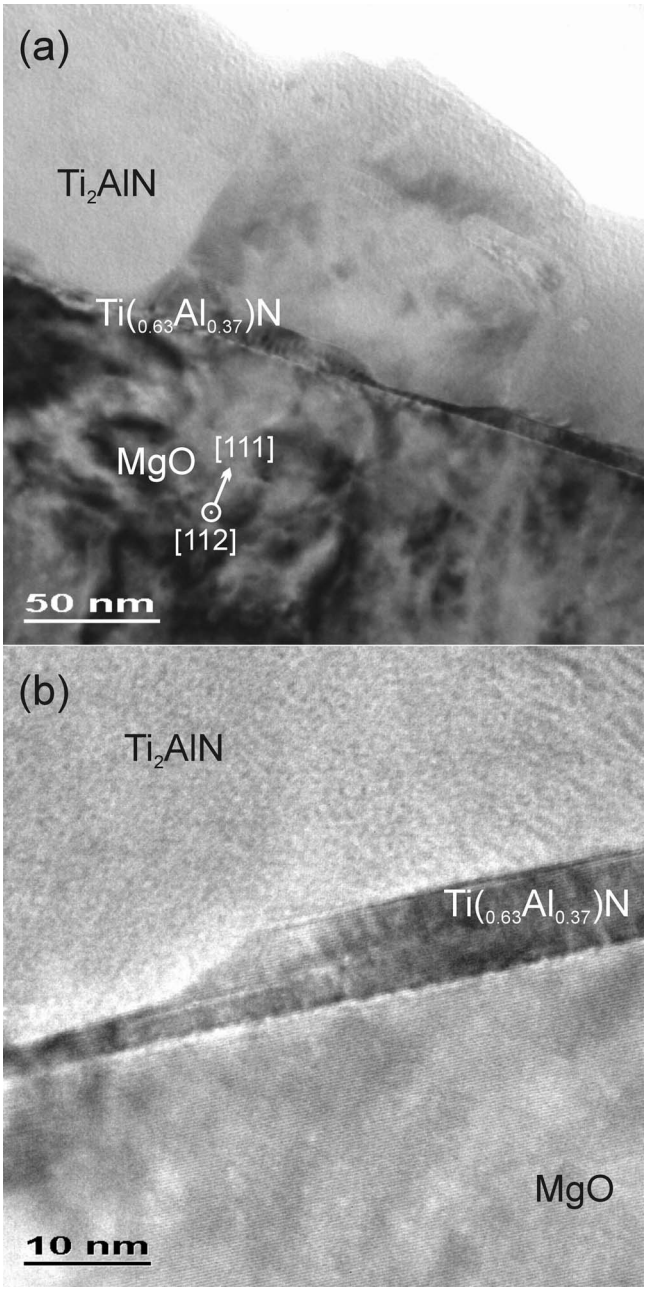

FIG. 6. XTEM micrographs of the interface between Ti_2AlN *MAX* phase, $(Ti_{0.63}Al_{0.37})N$ seed layer and MgO(111) substrate along the MgO[112] zone axis. After initial nucleation, the Ti_2AlN phase apparently grows into the $(Ti_{0.63}Al_{0.37})N$ seed layer (a). The more detailed HR-XTEM shows the pseudomorphic epitaxial relationship between the $(Ti_{0.63}Al_{0.37})N$ and MgO(111) indicated by persistent lattice planes.

The tilted basal-plane nucleation and the growth of Ti_2AlN on the seed layer can be depicted from the layered 2-1-1 structure being typical for *MAX* phases. Lattice plane spacing calculations by fast Fourier transformation (FFT) on the layered feature confirm multiple (000ℓ) planes of Ti_2AlN [Fig. 5(c)]. The tilting angle of the basal planes towards the substrate surface is $\sim 70°$, in agreement with the pole figure measurements. Hence, each of the grains in Fig. 5(a) represents one possible in-plane orientation of the Ti_2AlN (0002) observed in the pole figure of Fig. 3(b).

Figure 6(a) shows the interface between another Ti_2AlN grain and the $(Ti_{0.63}Al_{0.37})N$ seed layer on MgO(111).

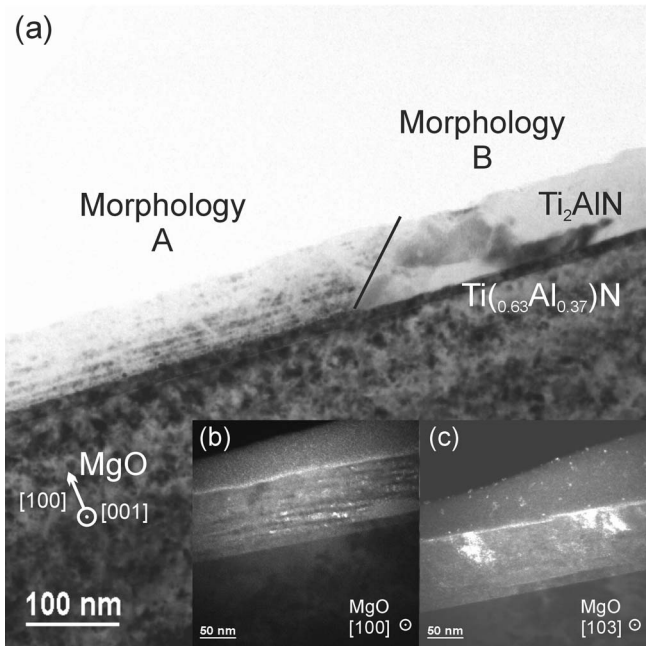

FIG. 7. (a) XTEM micrograph of Ti_2AlN grown on MgO(100) along the MgO[100] zone axis. The film shows two distinct morphologies, which represent two of the three possible orientations around the MgO[111] direction. (b) and (c) show dark field micrographs of the left morphology A along MgO[100] and MgO[103] zone axes, respectively.

Though the final seed layer thickness was 94 Å without significant deviation over the sample surface as proven by *in situ* XRR, i.e., immediately taken after deposition of the seed layer, here the interfacial layer occurs to be of irregular thickness. The more detailed high-resolution (HR)-XTEM micrograph in Fig. 6(b) suggests that this irregularity might stem from growth of the Ti_2AlN into the seed layer, leading to recrystallization and thus different diffraction contrast in XTEM. This could be a topotaxial effect by solid-state reaction that has also been shown for the growth of Ti_3SiC_2 onto MgO(100) by Emmerlich *et al.*[14] Nevertheless, the residual seed layer stays in perfect cube-cube epitaxial relationship to the MgO substrate, as indicated by the *d*-spacing fringes. According to the immediate onset of the intensity oscillations in specular reflectivity (Fig. 1), there is no indication towards a postponed nucleation of the Ti_2AlN seed layer, as has been observed for deposition of Ti_3SiC_2.[14]

The microscopic morphology of the Ti_2AlN changes completely, when deposited on MgO(100) as displayed in Fig. 7(a). Instead of equiaxed grains one can depict two distinct morphologies, a layered and a nonlayered structure both extending over the whole film thickness. The layered structure represents one-third of the aligned $Ti_2AlN(10\bar{1}3)$ cluster points of the pole figure around the fourfold possible MgO{111} points. The nonlayered morphology is due to grains turned by 120° around the MgO{111} and is accordingly not in diffraction contrast. Therefore, the same morphology can also be achieved by turning the cross-section sample around the MgO[111] direction.

Figure 7(b) shows a dark field micrograph of the layered structure along the MgO[100] zone axis. The light-dark contrast seen stems from the four possible MgO{111} orienta-

tions. Turning the sample by 18.2°, i.e., from one possible $Ti_2AlN(10\bar{1}3)$ grain population to the other [compare Fig. 4(b)], leads to the observation along the MgO[103] zone axis. As shown in the dark field micrograph of Fig. 7(c) the morphology now has changed completely from the layered structure to the nonlayered structure as equally observed in Fig. 7(a).

IV. DISCUSSION

Both the pole figure and XTEM results show that the orientational relationship between the MgO substrate and the Ti_2AlN *MAX* phase is $MgO\{111\}\langle 110\rangle // Ti_2AlN\{10\bar{1}2\} \times \langle \bar{1}2\bar{1}0\rangle$, regardless of substrate orientation. This is in contrast to the basal-plane growth of Ti_2AlN observed for growth at higher substrate temperatures.[16] It should be noted that the Ti_2AlN (0001) exhibits a nominal lattice mismatch of only 0.77% to the MgO(111) surface, as indicated in Figs. 8(a) and 8(b). As there are three $\langle 110\rangle$ directions on the MgO(111) surface, the Ti_2AlN may arrange itself in three possible orientations during the nucleation and initial stage of growth. When the film coalesces, adjacent grains of different orientations may adjoin [Fig. 8(b)] resulting in a final single-crystal film morphology as reported by Joelsson *et al.*[16] Hence the epitaxial relationship denotes as $MgO\{111\}\langle 110\rangle // Ti_2AlN\{0001\}\langle \bar{1}2\bar{1}0\rangle$. However, in our case the bonding of the Ti_2AlN to the MgO substrate and the $(Ti_{0.63}Al_{0.37})N$ seed layer is not given by the Ti_2AlN (0001), but the $Ti_2AlN(10\bar{1}2)$ plane, which projection is presented in Fig. 8(c). As is indicated by the polygon on the surface nitrogen atoms constituting this plane, a fitting on the MgO(111) surface along the $MgO\langle 110\rangle$ directions is possible, with the same nominal lattice mismatch of 0.77%. However, this prevents single-crystalline epitaxial growth for two reasons. First, an initial nucleation with threefold in-plane orientation [see Fig. 8(c)] does not allow coalescence at increasing film thickness. This is in agreement with the polycrystalline equiaxed morphology observed in XTEM, and also explains the threefold symmetry in the pole figure results.

Second, the adaptation of the $Ti_2AlN(10\bar{1}2)$ to the MgO(111) surface only occurs along one of the $MgO\langle 110\rangle$ directions. In the other corresponding $MgO\langle 110\rangle$ directions the adaptation can only be achieved by taking also over next surface nitrogen atoms into account, as shown by the polygon in Fig. 8(a). Still, in this direction the reconstruction shows a quite large misfit of 7.88–7.43 Å, corresponding to 6%. Besides, the cross-sectional view in Fig. 8(d) demonstrates that the interface cannot be configured only by Ti–N bondings, as it would be the case for basal-plane grown $Ti_2AlN(0001)//MgO(111)$. In fact, a ternary Ti–Al–N atomic reconfiguration also of more than nearest-neighbor atoms is necessary. This rather complicated and strained interfacial bonding could be attributed to the following. When depositing on the $(Ti_{0.63}Al_{0.37})N$ seed layer, its (111) surface in highly nitrogen-oversaturated gas mixtures tends to be N-terminated.[33] Comparing with Fig. 8(d), this implies that

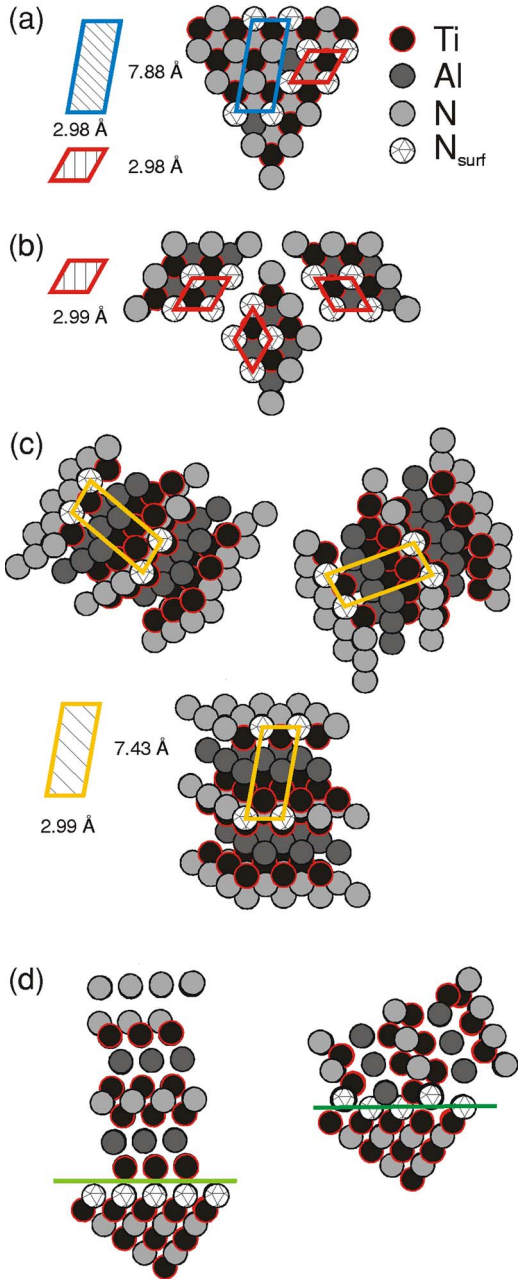

FIG. 8. (Color online) Atomic model illustration of the different $(Ti_{0.63}Al_{0.37})N$ and Ti_2AlN crystallographic planes and directions together with the geometric reconstructions for the pseudomorphic fitting of Ti_2AlN surfaces onto the $(Ti_{0.63}Al_{0.37})N$ (111) surface. (a) shows the $(Ti_{0.63}Al_{0.37})N$ (111) surface and (b) shows the three different $Ti_2AlN\langle \bar{1}2\bar{1}0\rangle$ orientations of the Ti_2AlN (0001) *MAX* phase basal plane along the $(Ti_{0.63}Al_{0.37})N\langle 110\rangle$ directions. (c) shows the same threefold $Ti_2AlN\langle \bar{1}2\bar{1}0\rangle$ orientations for the $Ti_2AlN(10\bar{1}2)$ planes. (d) shows cross-sectional views of the $Ti_2AlN/(Ti_{0.63}Al_{0.37})N$ interface for basal-plane and nonbasal-plane growths.

the initial atomic layer of Ti_2AlN (0001) has to consist purely of Ti atoms. However, the cosputtering process which is employed here provides an incoming flux of *both* Ti and Al atoms, so the initial elementary composition would need to be reconfigured. Moreover, this reconfiguration will be hindered, since the $(Ti_{0.63}Al_{0.37})N$ (111) surface is one with a relatively high adatom bonding energy and thus low mobility.[33] On top of this, the comparably low substrate tem-

peratures of only 690 °C will even aggravate this deficiency of adatom mobility. Hence, the texture evolution must be kinetically prevented from achieving maximum thermodynamic stability, e.g., basal-plane orientation. A deposition on MgO substrates *without* a $(Ti_{0.63}Al_{0.37})N$ seed layer, as reported by Joelsson *et al.*,[16] leads to different interfacial bonding possibilities, since for $Ti_2AlN(0001)//MgO(111)$, the MgO substrates offer the possibility of N–O surface bonds, but also a competing spinel-forming reaction.[34,35] Moreover, their deposition temperature of 830 °C with reported basal-plane growth of Ti_2AlN is significantly higher than the deposition temperature applied here, allowing for the correct partitioning of the elements at the substrate-film interface. The actual growth itself, however, will presumably still proceed in a step-flow type on the basal plane. As has been shown by means of atomic force microscopy for Ti_3SiC_2 by Emmerlich *et al.*,[14] high substrate temperature conditions lead to lateral growth of half and full unit cells. Incoming atoms diffuse on the (0001) plane until they find a step where they are bound to *a* facets. Decreasing the substrate temperature as in the present case causes different interfacial adaptation due to kinetical restrictions as described above. For both crystallographic orientations, however, growth still takes place on the same type of exposed surfaces, as can be deduced from XRR roughening and the morphology observed by XTEM.

V. SUMMARY

Ti_2AlN single-phase films have been deposited onto MgO(111) and MgO(100) single-crystal substrates at growth temperatures of 690 °C. The growth process has been characterized by *in situ* x-ray specular reflectivity and shows kinetic roughening of the developing films, which is more pronounced for the MgO(100) substrate orientation. The orientational relationship between MgO substrate and Ti_2AlN as derived by pole figure measurements is $MgO\{111\}\langle 110\rangle//Ti_2AlN\{10\bar{1}2\}\langle \bar{1}2\bar{1}0\rangle$, regardless of substrate orientation. This suggests a tilted, *non*-basal-plane growth of the Ti_2AlN which leads to a nonsingle- crystal morphology and rough, facetted surfaces as proven by XTEM. The nonbasal-plane growth can be explained in terms of insufficient adatom mobility during deposition leading to a kinetically restricted growth mode and to the observed *tilted* basal-plane growth. Work is in progress to investigate the influence of seed layer and the substrate temperature on the texture development of Ti_2AlN *MAX* phase thin films.

ACKNOWLEDGMENTS

We would like to thank U. Strauch for technical assistance during the measurements. Thanks are also due to J. Fassbender and J. Grenzer from Forschungszentrum Rossendorf and J. Emmerlich and T. Joelsson from Linköping University for fruitful discussions. Financial support from the Deutsche Forschungsgemeinschaft under Contract No. SCHE 682 is gratefully acknowledged.

[1] M. W. Barsoum and T. El-Raghy, J. Am. Ceram. Soc. **79**, 1953 (1996).
[2] W. Jeitschko, H. Novotny, and F. Benesovsky, Monatsch. Chem. **94**, 1198 (1963).
[3] J. J. Nickl, K. K. Schweitzer, and P. Luxenberg, J. Less-Common Met. **26**, 283 (1972).
[4] M. W. Barsoum, Prog. Solid State Chem. **28**, 201 (2000).
[5] http://www.3one2.com
[6] J. C. Schuster and J. Bauer, J. Solid State Chem. **53**, 260 (1984).
[7] M. W. Barsoum, L. Farber, I. Levin, A. Procopio, T. El-Raghey, and A. Berner, J. Am. Ceram. Soc. **82**, 2545 (1999).
[8] B. Holm, R. Ahuja, S. Li, and B. Johansson, J. Appl. Phys. **91**, 9874 (2002).
[9] D. Music, Z. M. Sun, and J. M. Schneider, Phys. Rev. B **71**, 052104 (2005).
[10] Z. M. Sun, D. Music, R. Ahuja, S. Li, and J. M. Schneider, Phys. Rev. B **71**, 059903 (2005).
[11] T. Seppänen, J.-P. Palmquist, P. O. Å. Persson, J. Emmerlich, J. Molina, J. Birch, U. Jansson, P. Isberg, and L. Hultman, *Proceedings of the 53rd Annual Meeting of the Scandanavian Society for Electron Microscopy*, Tampere, Finland, 12–15 June, 2002, edited by J. Kerýnen and K. Sillanpýý (University of Tampere Press, Tampere, 2002), pp. 142–143.
[12] J.-P. Palmquist, U. Jansson, T. Seppänen, P. O. Å. Persson, L. Hultman, and P. Isberg, Appl. Phys. Lett. **81**, 835 (2002).
[13] O. Wilhelmsson, J.-P. Palmquist, T. Nyberg, and U. Jansson, Appl. Phys. Lett. **85**, 1066 (2004).
[14] J. Emmerlich, H. Högberg, S. Sasvári, P. O. Å. Persson, L. Hultman, J.-P. Palmquist, U. Jansson, J. M. Molina-Aldareguia, and Z. Czigány, J. Appl. Phys. **96**, 4817 (2004).
[15] H. Högberg, P. Eklund, J. Emmerlich, J. Birch, and L. Hultman, J. Mater. Res. **20**, 779 (2005).
[16] T. Joelsson, A. Hörling, J. Birch, and L. Hultman, Appl. Phys. Lett. **86**, 111913 (2005).
[17] W. Matz, N. Schell, W. Neumann, J. Bøttiger, and J. Chevallier, Rev. Sci. Instrum. **72**, 3344 (2001).
[18] M. Beckers, N. Schell, R. M. S. Martins, A. Mücklich, and W. Möller, J. Vac. Sci. Technol. A **23**, 1384 (2005).
[19] N. Grandjean, J. Massies, P. Vennegues, M. Leroux, F. Demangeot, M. Renucci, and J. Frandon, J. Appl. Phys. **83**, 1379 (1998).
[20] E. Weschke, C. Schüssler-Langeheine, R. Meier, G. Kaindl, C. Sutter, D. Abernathy, and G. Grübel, Phys. Rev. Lett. **79**, 3954 (1997).
[21] J. Bøttiger, J. Chevallier, J. H. Petersen, N. Schell, W. Matz, and A. Mücklich, J. Appl. Phys. **91**, 5429 (2002).
[22] http://www.rzg.mpg.de/~mam/
[23] B. O. Johansson, J.-E. Sundgren, J. E. Greene, A. Rockett, and S. A. Barnett, J. Vac. Sci. Technol. A **3**, 303 (1985).
[24] P. B. Mirkarimi, M. Shinn, and S. A. Barnett, J. Vac. Sci. Technol. A **10**, 75 (1992).
[25] S. Kodambaka, V. Petrova, A. Vailionis, P. Desjardins, D. G. Cahill, I. Petrov, and J. E. Greene, Thin Solid Films **392**, 164 (2001).
[26] S. Kodambaka, S. V. Khare, W. Święch, K. Ohmori, I. Petrov, and J. E. Greene, Nature (London) **429**, 49 (2004).
[27] http://www.bede.co.uk
[28] U. Wahlström, L. Hultman, J.-E. Sundgren, F. Adibi, I. Petrov, and J. E. Greene, Thin Solid Films **235**, 62 (1993).
[29] A. Madan, I. W. Kim, S. C. Cheng, P. Yashar, V. P. Dravid, and S. A. Barnett, Phys. Rev. Lett. **78**, 1743 (1997).
[30] JCPDS Powder Diffraction File-International Center for Diffraction Data, Park Lane, Swarthmore PA, USA, Card No. 45-0946.
[31] M. Y. Gamarnik, M. W. Barsoum, and T. El-Raghy, Powder Diffr. **15**, 241 (2000).
[32] http://pro.wanadoo.fr/carine.crystallography/index.html
[33] D. Gall, S. Kodambaka, M. A. Wall, I. Petrov, and J. E. Greene, J. Appl. Phys. **93**, 9086 (2003).
[34] L. Hultman, J.-E. Sundgren, and D. Hesse, J. Mater. Res. **4**, 1266 (1989).
[35] L. Hultman, D. Hesse, and W.-A. Chiou, J. Mater. Res. **6**, 1744 (1991).